# Visual and Quantitative Analysis of Great Arteries' Blood Flow Jets in Cardiac 4D PC-MRI Data

Benjamin Köhler, Matthias Grothoff, Matthias Gutberlet, Bernhard Preim



DOI: 10.1111/cgf.13412

Eurographics Conference on Visualization (EuroVis) 2018
J. Heer, H. Leitte, and T. Ropinski
(Guest Editors)

*Volume 37 (2018), Number 3*

# Visual and quantitative analysis of great arteries' blood flow jets in cardiac 4D PC-MRI data

B. Köhler[1] and M. Grothoff[2] and M. Gutberlet[2] and B. Preim[1]

[1]Dept. of Computer Graphics and Simulation, Magdeburg University, Germany
[2]Dept. of Diagnostic and Interventional Radiology, Heart Center Leipzig, Germany

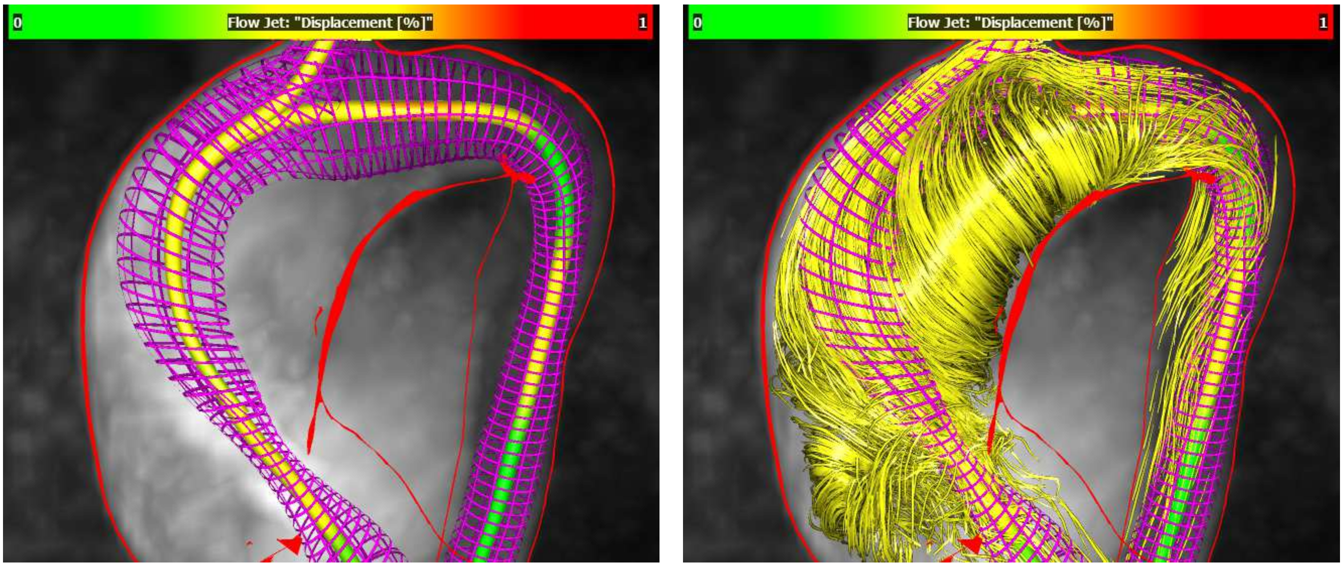


(a) (b)

**Figure 1:** *Patient with ascending aorta aneurysm. a) Our time-dependent visualization of the flow jet position (colored tube) and* ***area of the** 20 % **highest velocities*** *(**magenta net**) during peak systole. b) Combined visualization with vortex flow.*

**Abstract**

*Flow in the great arteries (aorta, pulmonary artery) is normally laminar with a parabolic velocity profile. Eccentric flow jets are linked to various diseases like aneurysms. Cardiac 4D PC-MRI data provide spatio-temporally resolved blood flow information for the whole cardiac cycle. In this work, we establish a time-dependent visualization and quantification of flow jets. For this purpose, equidistant measuring planes are automatically placed along the vessel's centerline. The flow jet position and region with highest velocities are extracted for every plane in each time step. This is done during pre-processing and without user-defined parameters. We visualize the main flow jet as geometric tube. High-velocity areas are depicted as a net around this tube. Both geometries are time-dependent and can be animated. Quantitative values are provided during cross-sectional measuring plane-based evaluation. Moreover, we offer a plot visualization as summary of flow jet characteristics for the selected plane. Our physiologically plausible results are in accordance with medical findings. Our clinical collaborators appreciate the possibility to view the flow jet in the whole vessel at once, which normally requires repeated pathline filtering due to varying velocities along the vessel course. The overview plots are considered as valuable for documentation purposes.*

Categories and Subject Descriptors (according to ACM CCS): Computing Methodologies [I.4.9]: Image Processing and Computer Vision—Applications • Computer Applications [J.3]: Life and Medical Sciences—

## 1. Introduction

4D phase-contrast magnetic resonance imaging (4D PC-MRI) [WSW96] enables the measurement of spatio-temporally resolved blood flow directions of one heart beat. These comprehensive flow information have been a valuable asset for a deeper understanding of the role of hemodynamics in the genesis and evolution of cardiovascular diseases. Qualitative data analysis is facilitated via flow visualization techniques like pathlines. Various quantitative measures can be obtained as well, such as flow volumes, shear forces on the vessel wall, and relative blood pressure. Though, 4D PC-MRI is not in the clinical routine yet. The evaluation of such data is an ongoing research topic.

Flow in the heart's great arteries, namely the aorta and pulmonary artery, is typically laminar. It straightly follows the vessel course with the highest velocities – *the flow jet* – located in the center (parabolic profile). Eccentric flow jets can be an indicator for different cardiovascular pathologies [RBM*18]. Among others, they have been linked to increased aneurysm growths in bicuspid aortic valve patients. In this malformation, two of the three aortic valve leaflets are fused, which leads to an altered opening behavior and the formation of vortex flow behind the valve [BM11]. Recent medical works quantify flow jets in cross-sectional measuring planes according to their displacement (eccentricity) [SDW*15], angle to the centerline [dSv*10], and size of the region with highest velocities [KKB*15]. This was carried out for the peak-systolic time step, when the pumped blood flow rate is maximal.

High-velocity pathlines are used for qualitative flow jet evaluation (see Fig. 2a). However, variations along the vessel make it impossible to find a suitable velocity threshold that shows the flow jet for the whole vessel at once. Instead, repeated filtering is necessary for each vessel section. In this paper, we propose a fully automated, adaptive extraction of time-resolved flow jet information. We start with placing equidistant measuring planes along the full centerline. For each plane, the flow jet position and the area that is occupied by high velocities are obtained in every temporal position. Based on this, the flow jet is visualized as geometric tube colored according to the flow displacement. High-velocity areas are depicted as a net around this tube. Both can be viewed simultaneously and in combination with pathlines, e.g., of extracted vortex flow [BPM*13] (see Fig. 1). The time-dependent geometries can be animated. Quantitative flow jet information can be obtained by evaluating cross-sectional measuring planes. Moreover, we provide a plot visualization as an overview of the flow jet characteristics in one cross-section.

Our main contributions are:

- We automatically extract the flow jet position and area of highest velocities for the whole vessel. Time-dependent, geometric visualizations are established for both.
- We propose a two-dimensional plot visualization as summary of the flow jet behavior in one cross-sectional measuring plane.

## 2. Related Work

This section summarizes related works regarding 4D PC-MRI, flow jet quantification in these data, and general flow abstraction.

**4D PC-MRI**: Stankovic et al. [SAG*14] and Nayak et al. [NNB*15] provide overviews about 4D flow MRI. Dyverfeldt and colleagues [DBB*15] published a comprehensive consensus article with shared experiences. Hope et al. [HSD13] and Calkoen et al. [CRV*14] focus on clinical applications and utility for diagnosing related cardiovascular diseases. In their more technical survey about the 4D PC-MRI data processing pipeline, Köhler et al. [KBV*17] classified quantification techniques into three categories. Cross-sectional methods are based on measuring planes that typically lie in the vessel's cross-section (perpendicular to the centerline). Surface- and grid-based measures are calculated on the vessel surface and in the image data grid, respectively.

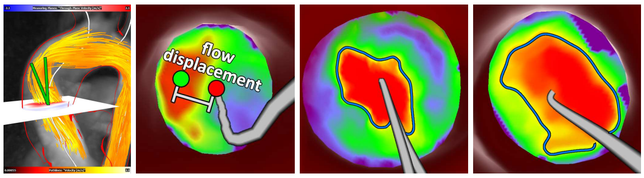


(a) (b) (c) (d)

**Figure 2:** *a) Flow jet to centerline* ***angle*** *(**green**). b–d) Measuring plane, orthogonal to the aorta's* ***centerline*** *(**gray**), with sampled velocities (rainbow color scale). Flow displacement (b) as distance between the* ***centerline position*** *on the plane (**red**) and the* ***velocity-weighted plane center*** *(**green**). Small (c) and large (d)* ***high-velocity area*** *(**blue contour**).*

**4D PC-MRI Flow Jet Quantification**: Den Reijer et al. [dSv*10] evaluated angles between the vessel centerline and main blood flow jet from the left ventricle through the aortic valve into the aorta (see Fig. 2a). This was used, e.g., as a measure for the reproducibility of 4D flow quantification [DHS*13]. Sigovan et al. [SDW*15] refer to this measure as *flow jet angle*.

Furthermore, Sigovan et al. define *flow displacement* as a relative, cross-sectional measure. It is the distance between the velocity-weighted measuring plane center and the vessel center, normalized with the vessel radius (see Fig. 2b). Eccentric flow jets were observed by Hope et al. [HHM*10] in bicuspid aortic valve patients. This was linked to aneurysm growth [HWS*12].

Kari et al. [KKB*15] proposed *flow compression index* as ratio between the area occupied by peak-systolic high velocities and the vessel's cross-sectional area (see Figs. 2c–d).

**Flow Abstraction**: Born et al. [BMGS13] proposed a generic simplification of 4D PC-MRI flow features, e.g., high-velocity or vortex flow, extracted with line predicates [BPM*13, KGP*13, JERH16]. The line bundles are smoothed to decrease complexity, then voxelized and skeletonized (thinning). A minimal subset of representative lines is determined that visit each voxel of the skeleton. These lines are visualized as stream tape with arrow head glyphs. Similar courses are fused. The original voxelization size is indicated as light gray surrounding. Temporal information are not incorporated. Also, connectivity and appearance of the static glyph strongly depend on the voxelized lines.

Gasteiger et al. [GLV*12] extracted flow jets in cerebral aneurysms using simulated computational fluid dynamics (CFD) data. A characteristic of this particular anatomical context is that there is no clear vessel course due to the often spherical shapes

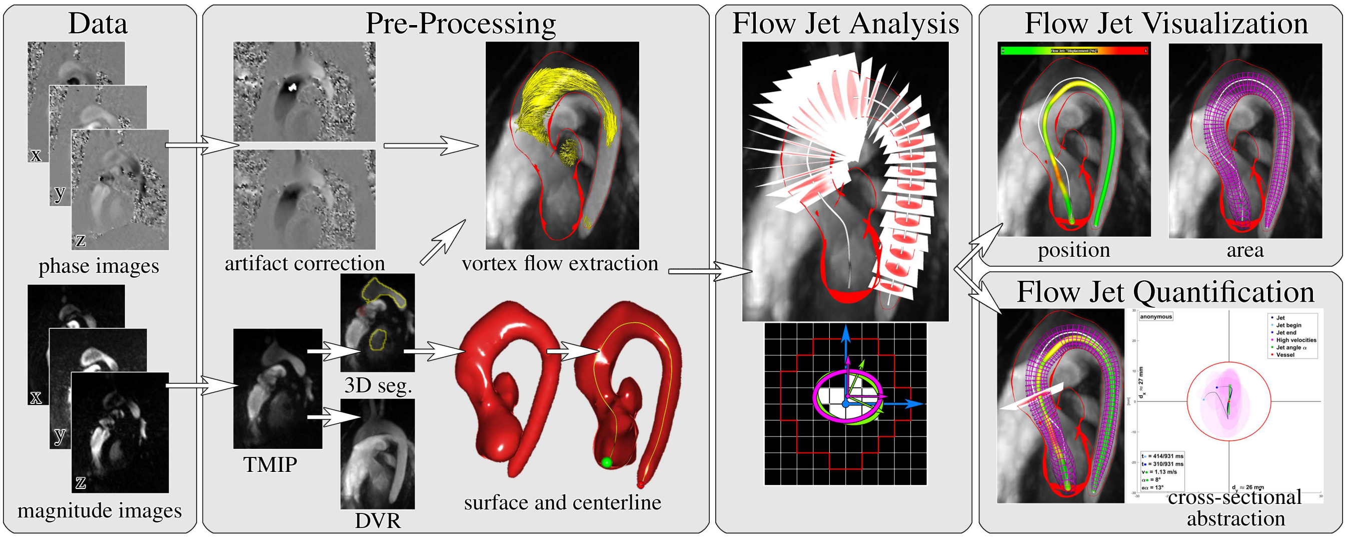


**Figure 3:** *Processing pipeline overview. The phase (flow) images are automatically corrected and then used for flow integration and vortex extraction. A temporal maximum intensity projection (TMIP) is performed on the magnitude images. This serves as anatomical context via direct volume rendering (DVR) and as basis for a 3D vessel segmentation. The subsequently extracted surface and centerline are employed in the measuring plane-based extraction of flow jet information. Time-dependent, geometric visualizations are established. Measuring planes facilitate flow jet quantification. A cross-sectional abstraction of flow jet characteristics is created as overview.*

of cerebral aneurysms. However, there is an ostium: A curved plane that separates vessel and aneurysm. The authors determine a stream surface, seeded on the ostium plane, that fulfills several criteria as good as possible: It comes close to the impingement zone (where the flow jet hits the vessel wall), it has a strong acceleration magnitude, and it shows a rapid change in flow direction. The inflow jet, as a simplified version of the extracted stream surface, is visualized as view-aligned arrow glyph.

Other methods rely on flow field or line clustering and finding representative lines per cluster. Yu et al. [YWM07] subdivided 4D vector fields using adaptive octrees. Van Pelt et al. [VJtV12] used a 4D spatio-temporal clustering for this purpose. Englund et al. [ERH16] placed a measuring plane in the ascending aorta, calculated finite-time Lyapunov exponents (FTLE), and clustered those values. All three methods calculate one or more representative pathlines afterwards for each cluster. Oeltze et al. [OLK*14] filled the whole 3D domain in CFD data of cerebral aneurysms with streamlines and clustered them according to different measures regarding the flow field (e.g., velocity, pressure), line geometry (e.g., curvature), or vessel (e.g., vessel wall distance). A representative streamline per cluster was selected that has, on average, the smallest distance to all other lines.

## 3. Data Acquisition and Pre-Processing

Our processing pipeline is summarized in Fig. 3. The data were acquired with a 3 T Siemens Magnetom Verio MR scanner by our clinical collaborators from the Heart Center in Leipzig, Germany. The 4D image grid sizes are between 132–144 columns, 192 rows, 15–72 slices, and 14–23 time steps. Especially the slice number variation is due to incremental updates of the employed scan sequence. The corresponding spatial resolutions are about $1.8 \times 1.8 \times 1.8$–$3.5$ mm/40–60 ms. The expected maximum velocity ($V_{\mathrm{enc}}$, a pre-scan parameter) was chosen depending on the patient-specific situation between 1.5 m/s (healthy aorta) and 3.0 m/s (faster flow due to stenosis / narrowing). Phase wraps, an image artifact where velocities seemingly flip, can occur if $V_{\mathrm{enc}}$ was underestimated. Thus, the obtained phase images (flow images) were corrected with a 4D phase unwrapping [LSJW15].

A temporal maximum intensity projection (TMIP) was performed on the three magnitude images. They contain undirected flow directions with less noise than the phase images. On this magnitude TMIP, which shows the highest velocities per pixel during the heart beat, a 3D vessel segmentation was performed using a graph cut [BK04, LS10]. Time-dependent segmentations on the flow data are not feasible since image contrast directly depends on flow velocities, i.e., the contrast in the arteries is high and low during systole and diastole, respectively. A vessel surface is then extracted via marching cubes and post-processed with a volume-preserving $\lambda/\mu$ Laplacian smoothing [TZG96]. Centerline extraction is based on minimum cost paths on an intravascular vessel wall distance map between two user-given points. This also provides a vessel radius estimation per centerline point.

Pathlines are the common choice for blood flow visualization in the medical community due to their intuitive interpretability. Thus, we integrate 30.000 uniformly distributed pathlines within the vessel segmentation using Runge-Kutta 4. Line predicate-based filtering [BPM*13, JERH16] allows to extract features like vortex flow [KGP*13].

## 4. Blood Flow Jets in Great Arteries

**Terminology**: We use the following terms:

- *Flow jet position* refers to the position in a cross-sectional measuring plane.

- *Flow displacement* is equivalent to *flow eccentricity*.
- *Flow jet area* describes the cross-sectional region that is occupied by the highest $x$ % of the velocities.
- *Flow compression index* is the flow jet area's portion of the cross-sectional area.

**Measuring Planes**: The basis for our method are equidistant measuring planes along a centerline. 2.5 mm is used as empirically determined default distance parameter in the context of the typically 30–40 cm long aorta (discussion in Sec. 8.2). A plane consists of:

- The *center* $\vec{c} \in \mathbb{R}^3$ equals the centerline position.
- The *normal vector* $\vec{n}_z \in \mathbb{R}^3$ corresponds to the normalized centerline tangent at $\vec{c}$. It is ensured that each centerline follows the natural vessel course, i.e., the tangents point in direction of the main flow.
- A *local coordinate system* $\vec{n}_x$, $\vec{n}_y \in \mathbb{R}^3$ spans the plane in the vessel's cross-section where $\vec{n}_{\{x,y,z\}}$ are orthonormal. Local coordinate systems between subsequent measuring planes have a consistent orientation, as described in [KPG*16].
- The *grid size* $\vec{g} = (g_x, g_y, g_t)$, $g_{\{x,y,t\}} \in \mathbb{N}^+$ specifies the plane's number of grid points. It can be seen as a 2D+time image. $g_t$ equals the dataset's number of time steps. We use $g_{\{x,y\}} = 50$ as default. About half of the 2500 grid points are within the 2.5–3.5 cm wide aorta per time step.
- The *scale* $\vec{s} = (s_x, s_y, s_t)$, $s_{\{x,y,t\}} \in \mathbb{R}$, $x,y,t > 0$ defines the spatio-temporal size of each rectangular cell. $s_{\{x,y\}}$ are set to 2.5× the vessel radius at the current centerline position so that the plane slightly protrudes the vessel. $s_t$ equals the dataset's temporal resolution.
- A *cross-sectional segmentation* $S$ is obtained by rasterizing the extracted vessel surface on the grid.

## 5. Requirements

From discussions with our clinical collaborators, who are also co-authors of this paper, we derived the following medical requirements:

*MR1*: Both qualitative and quantitative flow jet evaluation should be facilitated. Simultaneous depiction of the flow jet size and position is wanted.

*MR2*: Overly complex visualizations without additional benefit lead to lower method acceptance. Simplicity and appropriateness are preferred.

*MR3*: Flow displacement and flow jet angle are most interesting. Rough estimations for the flow compression index are sufficient.

*MR4*: Peak-systolic values, when the flow jet is at its maximum velocity, are considered as most important. Diastolic values are less interesting. A main interest is the systolic inflow jet, i.e., jet parameters above the aortic valve.

We add the following technical requirements:

*TR1*: A flow jet representation as explicit, time-dependent line is desired. It enables straight-forward calculation of flow displacement and angles to the centerline.

*TR2*: As our main targeted user group are cardiologists and radiologists, reasonable default parameters should be provided whenever possible to facilitate ease of use.

## 6. Flow Jet Extraction

In this section, we describe the flow jet extraction. In case of branching vessels, each centerline is processed individually.

### 6.1. Position

The flow jet position $\mathrm{FJ}_{\mathrm{pos}}(t)$ is determined for each temporal position $t$ as velocity-weighted measuring plane center within the cross-section segmentation $S$. More precisely, it is a summation of the grid positions' coordinates $MP(x,y)$ with weights according to the velocity vector lengths $\| \vec{v}_t \|$, sampled from the flow field via trilinear interpolation:

$$\mathrm{FJ}_{\mathrm{pos}}(t) = \frac{\sum\limits_{\forall x}\sum\limits_{\forall y}\Big(S(x,y)\cdot weight(\vec{v}_t)\cdot MP(x,y)\Big)}{\sum\limits_{\forall x}\sum\limits_{\forall y}\Big(S(x,y)\cdot weight(\vec{v}_t)\Big)} \tag{1}$$

$$\text{with}\quad S = \begin{cases} 1 & \text{, if } (x,y) \text{ inside segmentation} \\ 0 & \text{, else.} \end{cases},$$

$$MP(x,y) = \vec{c} + \Big(s_x\cdot\vec{n}_x\cdot(x-\frac{g_x}{2}) + s_y\cdot\vec{n}_y\cdot(y-\frac{g_y}{2})\Big),$$

$$weight(\vec{v}_t) = \begin{cases} \| \vec{v}_t \|^k & \text{, if forward flow } (\vec{v}_t\cdot\vec{n}_z > 0) \\ 0 & \text{, else.} \end{cases}.$$

We use the velocity weight function $weight(\vec{v}_t)$ with $k = 10$ (cf. TR2) to strongly favor high velocities. Classic mean value calculation may drag the flow jet position too much towards the vessel center and thus underestimate the flow displacement.

Backwards oriented flow can occur during diastole or when a measuring plane is slicing a certain type of vortex flow. Incorporating these positions would lead to wrong calculation of the flow jet. Therefore, grid positions $(x,y)$ are only taken into account if $\vec{v}_t\cdot\vec{n}_z > 0$, i.e., $\vec{v}_t$ points in direction of the measuring plane normal. If all sampled velocity vectors on a measuring plane at a time step point in backwards direction, no $\mathrm{FJ}_{\mathrm{pos}}(t)$ will be obtained. The centerline position will be used as result in this case to avoid discontinuities. This occurs rarely (see Sec. 8) and thus is not explicitly indicated by the visualization.

We would like to emphasize the importance of the phase unwrapping pre-processing step. Otherwise, the highest, most important velocities could be excluded from the calculation.

### 6.2. Area

For each temporal position $t$, the flow jet area is the set of pixels on a measuring plane with the $x$ % highest velocities. Velocities vary along the vessel and over time. For example, there might be a fast inflow jet through the aortic valve, but much lower velocities in the descending aorta. Thus, velocity thresholding within the whole aorta is not sufficient. Instead, relative velocities $v_t^{\mathrm{rel}}$ are required. For each measuring plane, we determine the maximum velocity $v_t^{\mathrm{max}}$. The 99 % quantile is used to increase robustness against potential outliers. $v_t^{\mathrm{max}}$ is used for normalization of velocities $\| \vec{v}_t \|$:

$$v_t^{\mathrm{rel}} = \frac{\min(\| \vec{v}_t \|,\, v_t^{\mathrm{max}})}{v_t^{\mathrm{max}}} \tag{2}$$

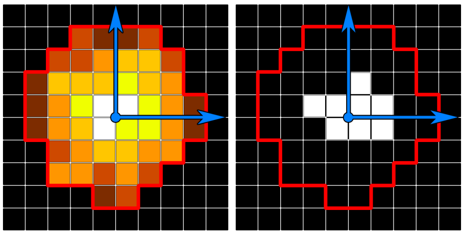

(a) (b)

**Figure 4:** *a) Schematic measuring plane grid with forward velocity vector magnitudes in a heat color scale. The* ***blue vectors*** *are the* ***plane's local coordinate system****,* ***red*** *is the rasterized* ***vessel boundary****. b) Mask (white) of the highest velocities.*

A mask is obtained via thresholding $v_t^{\text{rel}} \geq 0.8$ (our default, cf. TR2, derived from discussions with our clinical collaborators), i.e., the 20 % highest velocities per measuring plane per time step are extracted (see Fig. 4). The mask's size divided by the segmentation size yields the flow compression index.

We perform a principal component analysis (PCA) of the mask's non-zero grid positions. This yields two eigenvectors and eigenvalues $(\vec{e}_0/\lambda_0,\ \vec{e}_1/\lambda_1)$ and a center of the flow jet area, representing an ellipse.

### 6.3. Data Structure

For each processed measuring plane we store:

- the measuring plane center $\vec{c}$,
- the vessel radius, and
- the local, orthonormal coordinate system $\vec{n}_{\{x,y,z\}}$, where $\vec{n}_z$ is the plane's normal vector.

In addition, for each temporal position we store:

- the flow jet position $\text{FJ}_{\text{pos}}(t)$,
- the relative velocity $v_t^{\text{rel}}$ at $\text{FJ}_{\text{pos}}(t)$,
- the absolute velocity $\| \vec{v}_t \|$ at $\text{FJ}_{\text{pos}}(t)$,
- the area center, and
- the area's eigenvectors directions $\vec{e}_{\{0,1\}}$ and eigenvalues $\lambda_{\{0,1\}}$,
- the flow compression index,
- the flow jet angle as angle between $\vec{n}_z$ and the derivative of $\text{FJ}_{\text{pos}}(t)$, calculated via central differences,
- the flow displacement as Euclidean distance between $\vec{c}$ and $\text{FJ}_{\text{pos}}(t)$, normalized with the vessel radius.

The masks are no longer needed. Spatial and temporal predecessor and successor of each plane are fixed, so that the connectivity is implicitly given. For each separate time step, we apply a 1D binomial filter (kernel size 3, 15 iterations) to the jet positions, normalized velocities, area centers, and area eigenvectors and eigenvalues (cf. TR1, TR2).

### 6.4. Quantification

There is a series of values over time for the *flow displacement*, *flow jet angle*, and *flow compression index*. Our clinical collaborators consider peak-systolic values as crucial, when the flow jet is at its maximum velocity (cf. MR4). Moreover, we derived that importance is linked to velocities. Thus, we also provide velocity-weighted mean values.

Quantitative values for one cross-section can be obtained using a measuring plane. The specified plane is likely to lie between two of the original measuring planes that were used during flow jet extraction. Linear interpolation of the flow jet properties (recall Sec. 6.3) is performed in these cases.

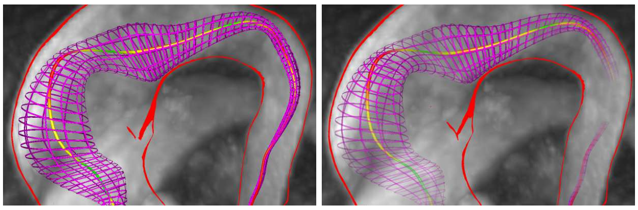

(a) (b)

**Figure 5:** *Flow jet of a patient with ascending aorta aneurysm during the end of systole without (a) and with (b) transparently fading out low velocities. The flow jet position tube is colored from green to yellow to red according to its displacement.*

## 7. Flow Jet Visualization

This section describes the flow jet visualization and animation.

### 7.1. Time-dependent, Three-dimensional Geometries

We propose a 3D+time geometric visualization for the flow jet position and area of highest velocities.

#### 7.1.1. Position

It is natural to visualize the series of flow jet positions as line. However, to make the flow jet appearance clearly distinctive from pathlines, which we render as view-aligned quads, we create a time-dependent, geometric tube. There is a local coordinate system for each position, allowing circular sampling in the plane around the plane normal. The coordinate systems' consistent orientations along the vessel course allow trivial triangulation of the tube without further correspondence analysis.

**Conveyed Measures**: The local radius of the tube is set to the velocity at the flow jet position, normalized with the maximum velocity in the whole vessel. This radius is scaled by 2 to make the jet appearance more prominent. Thus, the tube is thicker and thinner for fast and slow flow, respectively. Flow displacement (cf. MR3) are color-coded in a traffic light color scale (green to yellow to red).

**Velocity-based Fading**: With decreasing velocities, especially during diastole, the flow jet becomes less meaningful, as there is no more clear main direction. Therefore, we transparently fade out low velocities $v_t^{\text{rel}}$:

$$\alpha = \begin{cases} 1 & \text{, if } v_t^{\text{rel}} \geq a \\ \left(v_t^{\text{rel}} \ / \ a\right)^e & \text{, if } \varepsilon \leq v_t^{\text{rel}} < a \\ 0 & \text{, if } \varepsilon > v_t^{\text{rel}} \end{cases} \tag{3}$$

Our defaults (cf. TR2) are $a = 1/3$ and $e = 5$ (see Fig. 5). Values below $\varepsilon = 0.05$ are hidden completely.

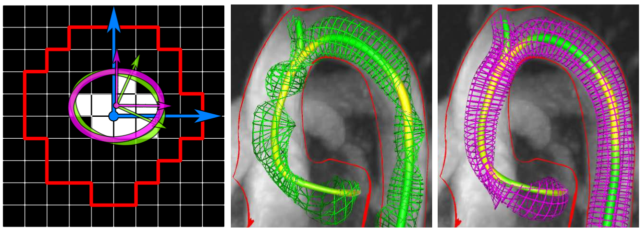

(a) (b) (c)

**Figure 6:** *a) Principal component analysis (PCA) of the mask (recall Fig. 4) within the rasterized **vessel boundary** (**red**). a–c) **Original area ellipses** (**green**) from the PCA and **approximate area ellipses** (**magenta**) with higher visual quality that are aligned with the **plane's local coordinate system** (**blue vectors**).*

### 7.1.2. Area

It should be possible to simultaneously evaluate the flow jet position and area (cf. MR1). The flow jet position tube is always inside the extracted area of highest velocities. We decided against a semi-transparent hull surface, since it changes the tube's color-coded displacement values. Instead, a net is used with two sets of orthogonally aligned lines. The first set are rings around the jet area, analogous to metal rings on a barrel. One ring is placed at each position where a measuring plane was during the jet extraction. The second are ten lines (our default, cf. TR2) that follow the course of the area. The lines are rendered as 0.5 mm wide quads that lie on the surface of the area hull.

**Area Ellipses**: The area ellipses are spanned by the two eigenvectors and eigenvalues obtained from the PCA. Unfortunately, there is no consistent orientation between eigenvectors of subsequent positions. This can cause many twists (see Fig. 6b).

From discussions with our clinical collaborators, we derived that rough estimations for the flow compression index are sufficient. It is more about getting an impression if the whole vessel is filled equally or if the distribution is skewed. Therefore, we altered the flow jet area depiction in favor of a more consistent visualization. We use the consistent local coordinate systems $\vec{n}_{\{x,y,z\}}$ and calculate the angles $\beta_x = |\vec{e}_0 \cdot \vec{n}_x|$ and $\beta_y = |\vec{e}_0 \cdot \vec{n}_y|$. The original area ellipse directions $\vec{e}_{\{0,1\}}$ and associated radii $\lambda_{\{0,1\}}$ are replaced with:

$$(\vec{e}_0/\lambda_0,\ \vec{e}_1/\lambda_1) \rightarrow \begin{cases} (\vec{n}_x/\lambda_0,\ \vec{n}_y/\lambda_1) & \text{, if } \beta_x < \beta_y \\ (\vec{n}_x/\lambda_1,\ \vec{n}_y/\lambda_0) & \text{, else.} \end{cases} \tag{4}$$

The effect of this replacement is shown in Fig. 6. The original area ellipse directions are rotated by maximum 45°.

The ellipses may protrude the vessel. We correct this in a post-processing step. The minimum distances $d_{\vec{e}_0}$ and $d_{\vec{e}_1}$ to the vessel wall in direction of $\pm\vec{e}_0$ and $\pm\vec{e}_1$, respectively, are determined. The ellipse radii are clamped accordingly as:

$$\lambda_0 = \min(\lambda_0,\ d_{\vec{e}_0}) \qquad \text{and} \qquad \lambda_1 = \min(\lambda_1,\ d_{\vec{e}_1}). \tag{5}$$

**Visualization Details**: The lines are rendered with black halos (contours) that occupy 10 % of the line width on each side. This facilitates the easier recognition of crossing relations.

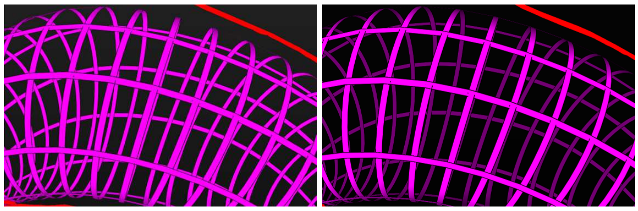

(a) (b)

**Figure 7:** *Flow jet area visualization without (a) and with (b) darkened back sides for improved recognition.*

We determined magenta as a suitable color in our context (cf. TR2). It has a good contrast to the grayish volume-rendered background and our default pathline color yellow, which we use, e.g., to show extracted vortex flow (see Fig. 1).

The area net is illuminated with the diffuse part of the Phong model. Absolute values of the normal vectors are used so that the back sides with normals facing away from the viewer do not appear black. We darken the colors of back sides by $1/3$ to improve the spatial perception (see Fig. 7).

### 7.1.3. Animation

The time-dependent position tube and area net geometries are animated using OpenGL's vertex shader. The shader receives the current animation time $t_{\text{anim}}$. For each vertex, a list of all its temporal positions $\vec{p}_t$ is stored in a shader storage buffer object (SSBO). The animated vertex position is linearly interpolated between $\vec{p}_{\lfloor t_{\text{anim}} \rfloor}$ and $\vec{p}_{\lceil t_{\text{anim}} \rceil}$.

## 7.2. Cross-sectional Flow Jet Characteristics

We propose a two-dimensional plot visualization that incorporates the previously discussed measures (see Fig. 8). It requires the specification of a cross-sectional measuring plane. One of our clinical collaborators' main interests are information about the systolic inflow jet, i.e., the jet parameters above the aortic valve. In a standard dataset evaluation, physicians place a measuring plane above the aortic valve to obtain the stroke volume (pumped blood volume per heart beat) which we can re-use for the plot.

**Vessel Context**: The vessel center lies in the plot origin. We determine two vessel radii for the specified cross-section as distance to the vessel wall in directions of the measuring plane's coordinate system. The vessel contour is then drawn as an ellipse. Its purpose is to assess relative positions of the other parameters like the flow jet position. We decided against using the actual cross-section segmentation. The limited spatial resolution could lead to irregular contours that unwantedly draw attention. The plot size is normalized so that there is a clearly visible diameter difference between, e.g., aneurysm patients and healthy volunteers. We allow a maximum vessel radius of 6 cm by default (cf. TR2). Thus, the x and y axes range from ±30 mm.

**Position**: Intersections of the flow jet position and the measuring plane over time are visualized as dark blue curve. We cut diastolic flow by excluding all flow jet positions with a velocity below the median flow jet velocity. The reasoning is the same as for the opacity reduction in the visualization (recall Sec. 7.1.1, cf. MR4).

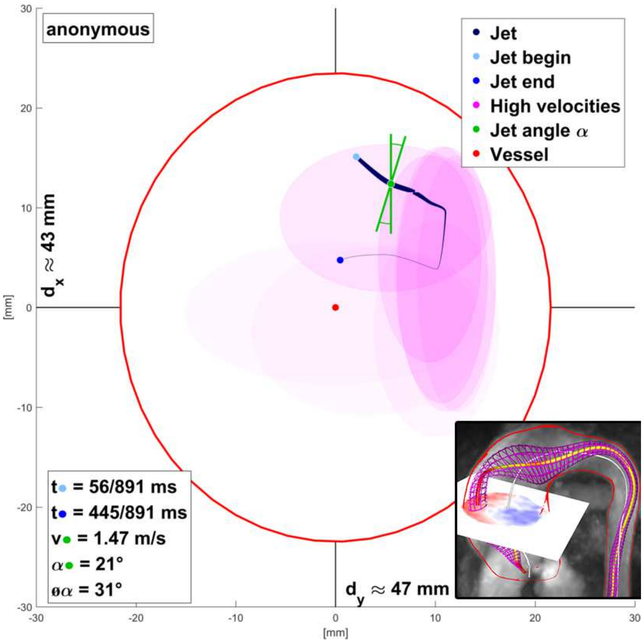


**Figure 8:** *2D plot visualization of an aneurysm patient's flow jet characteristics for one measuring plane (bottom right).*

The width $w_t$ of the dark blue curve is locally chosen according to the flow jet's relative velocity $v_t^{\mathrm{rel}}$ at the corresponding position and time as:

$$w_t = \max\left(0.01,\ (v_t^{\mathrm{rel}})^3\right). \tag{6}$$

The temporal development of the jet position starts and ends at the light and dark blue point, respectively.

**Angle**: The most important flow jet angle is the one at maximum velocity (cf. MR4). Therefore, we draw an angle glyph there in green. Only one glyph is used as multiple ones would quickly lead to visual clutter.

**Area**: The approximate area ellipses of all time steps are drawn semi-transparently for this specified cross-section. Opacities are weighted by the normalized flow jet velocity. This facilitates qualitative assessment of where the majority of fast flow passes.

**Labeling**: Top left is the dataset name. Vessel diameters are given on the middle left and bottom. The top right legend explains the visualization. The bottom left box contains precise values for the flow jet's start and end time, peak velocity, angle at the peak velocity position, and velocity-weighted average angle. The flow compression index is not given, as qualitative estimations are sufficient (cf. MR3). We inserted the bottom right image manually as a context.

## 8. Results

We evaluated the utility of our technique by applying it to 11 diverse, anonymized datasets of both healthy volunteers (4) as well as patients (6), and one of a flow phantom.

**Performance**: Our method was tested on an i7-3930K (6×3.2 GHz). The computational effort depends on the number of measuring planes that are evaluated along each centerline, which directly depends on the minimum distance parameter between subsequent planes. A second critical factor is the measuring plane grid size. Our default settings (2.5 mm distance, $50\times50$ grids, cf. TR2) yield 4–10 s flow jet calculation times. The computation is performed once as a pre-processing step after centerline extraction and artifact correction in the flow images.

**Visualization Discontinuities**: If no $\mathrm{FJ}_{\mathrm{pos}}(t)$ can be determined, the centerline position is used instead to avoid discontinuities in the visualization (recall Sec. 6.1). This occurred in $0.48\pm0.57$ % (mean $\pm$ standard deviation) of all time steps for all measuring planes in all datasets.

### 8.1. Qualitative Evaluation

This section describes results for both the proposed time-dependent geometries and the cross-sectional plots.

#### 8.1.1. Geometric Flow Jet Visualization

**Phantom**: This dataset of a straight flow phantom was used to validate our method. It is a flexible tube in a gel block in combination with a non-pulsatile water pump. In contrast to real, pulsatile datasets with strongly varying velocities, here we can find a global velocity threshold to extract the flow jet. Fig. 9a shows that the flow jet aligns well with the centerline and the flow jet area equally fills the tube as expected.

**Healthy Volunteer**: Fig. 9b shows a healthy volunteer during peak systole. The jet lies relatively in the middle of the vessel. In the aortic arch, there is slight, physiological helix flow that might cause the medium displacement. The cross-sections are consistently filled with high velocities, as indicated by the area net.

**Aneurysm Patient**: Fig. 9c is from a patient with an aneurysm in the ascending aorta (diameter ≈4.3 cm). The flow jet bypasses the large systolic vortex on the side and causes increased wall shear stress (WSS) on the vessel surface. This observation is in accordance with medical studies, e.g., by Barker et al. [BM11]. Absolute WSS values are usually underestimated by 4D PC-MRI due to the coarse resolution, but relativity is preserved, i.e., regions with significantly increased WSS can be determined [PMvN14].

**Age-related Vortex Flow**: The aorta of an elderly healthy volunteer is shown in Fig. 9d. Vortex flow in the ascending aorta could occur due to age-related, increased vessel wall stiffness, as described by Bogren and Buonocore [BB99]. Similar to Fig. 9c the main flow passes on the left side.

**BAV Patient**: The patient from Figs. 9g–j has a bicuspid aortic valve (BAV) with a severely widened ascending aorta (diameter ≈5 cm). Depending on which valve leaflets are fused, different vortex patterns can emerge [BHB*13]. Notice the positional flow jet changes during the cardiac cycle and how it keeps passing the vortex on the side.

**Aortic Arch Vortex**: The patient in Fig. 9e has a small vortex in the aortic arch. This causes increased flow displacement in this vessel section as well as a higher flow compression.

**Pulmonary Artery**: Fig. 9f shows the pulmonary artery of a healthy volunteer. We included this example to show that our method works for other tubular vessels as well.

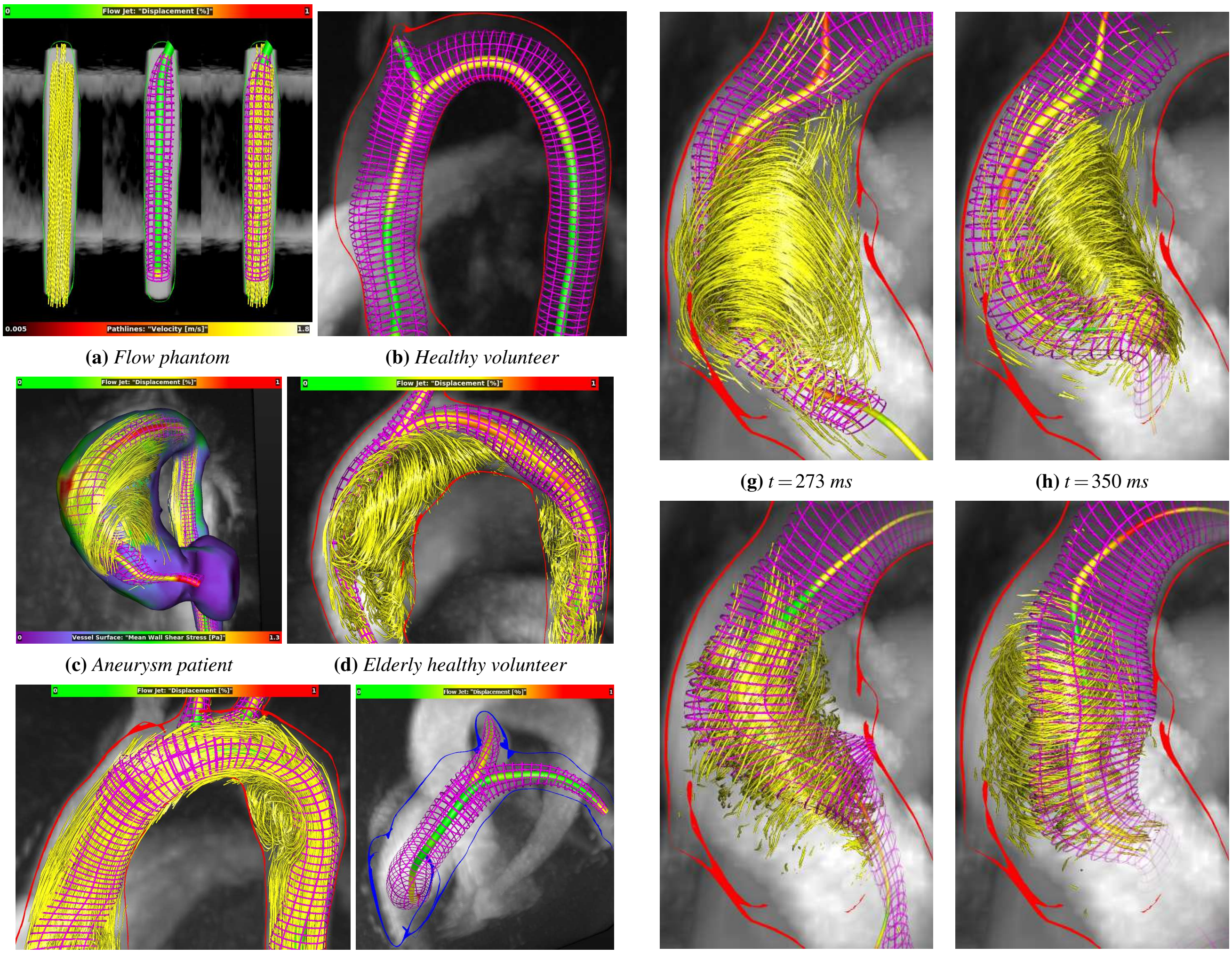


**(a)** *Flow phantom* **(b)** *Healthy volunteer* **(c)** *Aneurysm patient* **(d)** *Elderly healthy volunteer* **(e)** *Patient aorta* **(f)** *Healthy pulmonary artery* **(g)** $t = 273$ *ms* **(h)** $t = 350$ *ms* **(i)** $t = 417$ *ms* **(j)** $t = 550$ *ms*

**Figure 9:** *a) Non-pulsatile flow in a straight phantom. From left to right: High-velocity flow, our proposed flow jet visualization, combined view. b) Peak-systolic flow jet of a healthy volunteer. c) Patient with ascending aorta aneurysm and systolic vortex flow. The eccentric flow jet causes increased wall shear stress. d) Elderly healthy volunteer with vortex flow and peripheral flow jet in the ascending aorta vortex during systole. e) The flow jet bypasses the small vortex in this patient's aortic arch. f) Pulmonary artery of a healthy volunteer with each one flow jet for the branching left and right pulmonary artery. g–j) Development of the flow jet over the cardiac cycle ($T = 635$ ms) in a BAV patient with an ascending aorta aneurysm.*

#### 8.1.2. 2D Plot Visualization

The required measuring planes for the plots were re-used from stroke volume assessment above the aortic valve. Fig. 10 shows a healthy volunteer and a patient with an aortic valve defect as well as a pathologic vessel widening. The diameter differences are visible at first glance due to the normalized plot size. Notice how the healthy volunteer's flow jet resides in the middle of the aorta, whereas the patient's one is mainly located in the upper left cross-sectional region. The flow jet angles are $8^\circ$ (healthy volunteer) vs. $25^\circ$ (patient).

### 8.2. Discussion

In the majority of cases, the flow jet is most expressive during peak systole at its maximum velocity (cf. MR4). Our method could benefit from automatically finding this position. However, temporal development can be interesting as well (see Figs. 9g–j).

Slow, diastolic flow misses a clear main direction and thus is not expressive (cf. MR4). Our transparency fading successfully alleviates the problem. Carefully chosen parameter defaults were provided (cf. TR2).

Our method depends on the vessel segmentation and, more important, the specific course of the vessel centerline. Errors in one or the other may produce suboptimal results, e.g., as the calculation of the flow compression index directly depends on

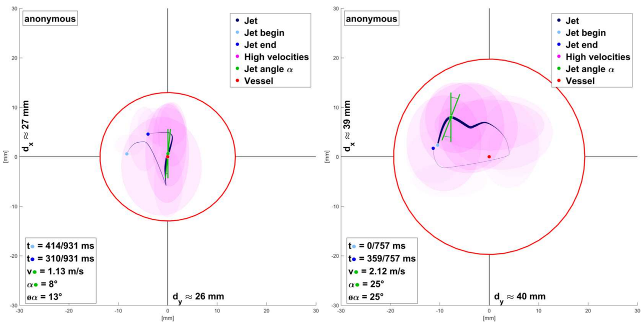


**(a)** *Healthy volunteer* **(b)** *Valve defect patient*

**Figure 10:** *Comparison of a healthy volunteer (a) and patient with pathologically widened aorta (b).*

the cross-sectional area. Also, our method requires tubular vessel shapes and may not work for roundish structures like ventricles.

The static approximation of the actually dynamic vessel inevitably leads to certain inaccuracies. This should be communicated, especially for the quantitative values.

During flow jet extraction, we use equidistant measuring planes with 2.5 mm distances on the centerline. Smaller values lead to an increased number of ellipses in the flow jet area visualization. At a certain density this will block the view inside. If our method shall be applied to, e.g., cerebral aneurysms, this parameter or the area net's line width needs to be re-adjusted to the new context.

The flow jet position tube, contrary to the area net, is often occluded in combined visualizations with vortex flow. Thus, flow should be hidden for qualitative flow displacement assessment. Alternatively, flow clustering approaches, e.g. by Oeltze et. al. [OLK*14], may be employed to reduce the scene complexity.

**Clinical Collaborators' Feedback**: On the first glance at the flow jet position tube, before any explanation and before reading the color bar title, our clinical collaborators interpreted the color-coding as velocities. However, they explicitly asked for flow displacement values and appreciated that it is already colored (cf. MR3). They find assessing the flow displacement more intuitive when simultaneously viewing the centerline by default and not on demand, as we currently do it in our system. The meaning of the magenta flow jet area net became clear when explained for a cross-section. In combined visualizations of extracted vortex flow, it can be hard to assess the color-coded flow displacement values from the flow jet position tube (cf. TR1). The magenta flow area nets are considered as more helpful in these cases. The overall visualization complexity was considered as appropriate (cf. MR2).

Fig. 9e shows an example where multiple flow jets overlap, each one for the main vessel course and for the branching vessels on top. This was not seen as disturbing.

The accuracy of visually assessing flow jet parameters was not considered as problematic, since precise values can easily be obtained when placing a measuring plane. These values can be found on the user interface in a statistics table where also, e.g., flow volumes are listed.

Contrary to our reasoning of avoiding potential distractions, the physicians would prefer to see the actual vessel contour in the plots. Still, the 2D plot visualization is highly appreciated, especially for a standardized patient documentation. However, an orientation or link to the 3D view is required.

## 9. Conclusion and Future Work

We extracted blood flow jets in great arteries from cardiac 4D PC-MRI data w.r.t. measures from current medical research. The whole computation is carried out in 4–10 s on the CPU in a one-time pre-processing step. We provide reasonable default parameters for the heart's great arteries, however, they may need to be re-adjusted in other domains like cerebral vessels.

We proposed a time-dependent, 3D geometric visualization for the flow jet position within the vessel and the area of highest velocities per cross-section. Contrary to threshold-based filtering of pathlines, this facilitates viewing the flow jet in the whole vessel at once. Moreover, we described a 2D plot visualization of flow jet characteristics for one cross-sectional measuring plane. Our methods were developed in close collaboration with radiologists with cardiovascular specialization and cardiologists. They found the 3D+time visualization most interesting in combination with extracted vortex flow, as one can easily see how the flow jet bypasses aberrant flow patterns. The 2D plot was considered as very beneficial for standardized documentation and report generation. Though, a patient-specific orientation or link to the 3D view needs to be added.

In the future, we could adapt our method to non-tubular vessels like the ventricles. Further performance tweaks are possible by incorporating the GPU. Our method could be applied to backward flow jets by inverting the order of the centerline points. This, however, raises numerous problems. There will be many temporal positions per plane where no backward flow exists. Our current solution for this rare situation of using the plane center will not be suitable here. Furthermore, the corresponding visualization needs to be clearly distinguishable from the forward flow jet. For the plots, we shall add the tilting direction of the flow jet angle.

## Acknowledgments

This work was funded by the German Research Foundation (PR 660/18-1). The authors thank B. Behrendt for fruitful discussions.

## References

[BB99] Bogren H. G., Buonocore M. H.: 4D magnetic resonance velocity mapping of blood flow patterns in the aorta in young vs. elderly normal subjects. *J Magn Reson Imag 10*, 5 (1999), 861–9. doi:10.1002/(SICI)1522-2586(199911)10:5<861::AID-JMRI35>3.0.CO;2-E. 7

[BHB*13] Bissell M. M., Hess A. T., Biasiolli L., Glaze S. J., Loudon M., Pitcher A., Davis A., Prendergast B., Markl M., Barker A. J., Neubauer S., Myerson S. G.: Aortic dilation in bicuspid aortic valve disease: Flow pattern is a major contributor and differs with valve fusion type. *Circ: Cardiovasc Imag 6*, 4 (2013), 499–507. doi:10.1161/CIRCIMAGING.113.000528. 7

[BK04] Boykov Y., Kolmogorov V.: An experimental comparison of min-cut / max-flow algorithms for energy minimization in vision. *IEEE TPAMI 26*, 9 (2004), 1124–37. doi:10.1109/TPAMI.2004.60. 3

[BM11] Barker A. J., Markl M.: The role of hemodynamics in bicuspid aortic valve disease. *Europ J Cardio-Thorac Surg 39*, 6 (2011), 805–6. doi:10.1016/j.ejcts.2011.01.006. 2, 7

[BMGS13] Born S., Markl M., Gutberlet M., Scheuermann G.: Illustrative visualization of cardiac and aortic blood flow from 4D MRI data. In *Proc: IEEE PacificVis* (2013), pp. 129–36. doi:10.1109/PacificVis.2013.6596137. 2

[BPM*13] Born S., Pfeifle M., Markl M., Gutberlet M., Scheuermann G.: Visual analysis of cardiac 4D MRI blood flow using line predicates. *IEEE TVCG 19* (2013), 900–12. doi:10.1109/TVCG.2012.318. 2, 3

[CRV*14] Calkoen E. E., Roest A. A. W., van der Geest R. J., De Roos A., Westenberg J. J. M.: Cardiovascular function and flow by 4-dimensional magnetic resonance imaging techniques: New applications. *J Thorac Imag 29*, 3 (2014), 185–96. doi:10.1097/RTI.0000000000000068. 2

[DBB*15] Dyverfeldt P., Bissell M., Barker A. J., Bolger A. F., Carlhäll C.-J., Ebbers T., François C. J., Frydrychowicz A., Geiger J., Giese D., Hope M. D., Kilner P. J., Kozerke S., Myerson S., Neubauer S., Wieben O., Markl M.: 4D flow cardiovascular magnetic resonance consensus statement. *J Cardiovasc Magn Reson 17*, 1 (2015), 1–19. doi:10.1186/s12968-015-0174-5. 2

[DHS*13] Dyverfeldt P., Hope M. D., Sigovan M., Wrenn J., Saloner D.: Reproducibility of quantitative analysis of aortic 4D flow data. *J Cardiovasc Magn Reson 15*, Suppl 1 (2013), P126. doi:10.1186/1532-429X-15-S1-P126. 2

[dSv*10] den Reijer P. M., Sallee D., van der Velden P., Zaaijer E. R., Parks W. J., Ramamurthy S., Robbie T. Q., Donati G., Lamphier C., Beekman R. P., Brummer M. E.: Hemodynamic predictors of aortic dilatation in bicuspid aortic valve by velocity-encoded cardiovascular magnetic resonance. *J Cardiovasc Magn Reson 12*, 4 (2010). doi:10.1186/1532-429X-12-4. 2

[ERH16] Englund R., Ropinski T., Hotz I.: Coherence maps for blood flow exploration. In *Proc: EG VCBM* (2016), p. epub. doi:10.2312/vcbm.20161274. 3

[GLV*12] Gasteiger R., Lehmann D. J., Van Pelt R. F. P., Janiga G., Beuing O., Vilanova A., Theisel H., Preim B.: Automatic detection and visualization of qualitative hemodynamic characteristics in cerebral aneurysms. *IEEE TVCG 18*, 12 (2012), 2178–87. doi:10.1109/TVCG.2012.202. 2

[HHM*10] Hope M. D., Hope T. A., Meadows A. K., Ordovas K. G., Urbania T. H., Alley M. T., Higgins C. B.: Bicuspid aortic valve: Four-dimensional MR evaluation of ascending aortic systolic flow patterns. *Radiol 255*, 1 (2010), 53–61. doi:10.1148/radiol.09091437. 2

[HSD13] Hope M. D., Sedlic T., Dyverfeldt P.: Cardiothoracic magnetic resonance flow imaging. *J Thorac Imag 28*, 4 (2013), 217–30. doi:10.1097/RTI.0b013e31829192a1. 2

[HWS*12] Hope M. D., Wrenn J., Sigovan M., Foster E., Tseng E. E., Saloner D.: Imaging biomarkers of aortic disease: Increased growth rates with eccentric systolic flow. *J Americ Coll Cardiol 60*, 4 (2012), 356–7. doi:10.1016/j.jacc.2012.01.072. 2

[JERH16] Jankowai J., Englund R., Ropinski T., Hotz I.: Interactive 4D MRI blood flow exploration and analysis using line predicates. In *Proc: SIGRAD* (2016), pp. 35–42. doi:10.13140/RG.2.1.4531.1607. 2, 3

[KBV*17] Köhler B., Born S., Van Pelt R. F. P., Hennemuth A., Preim U., Preim B.: A survey of cardiac 4D PC-MRI data processing. *CGF 36*, 6 (2017), 5–35. doi:10.1111/cgf.12803. 2

[KGP*13] Köhler B., Gasteiger R., Preim U., Theisel H., Gutberlet M., Preim B.: Semi-automatic vortex extraction in 4D PC-MRI cardiac blood flow data using line predicates. *IEEE TVCG 19*, 12 (2013), 2773–82. doi:10.1109/TVCG.2013.189. 2, 3

[KKB*15] Kari F. A., Kocher N., Beyersdorf F., Tscheuschler A., Meffert P., Rylski B., Siepe M., Russe M. F., Hope M. D.: Four-dimensional magnetic resonance imaging-derived ascending aortic flow eccentricity and flow compression are linked to aneurysm morphology. *Interact Cardiovasc Thorac Surg 20*, 5 (2015), 582–7. doi:10.1093/icvts/ivu446. 2

[KPG*16] Köhler B., Preim U., Grothoff M., Gutberlet M., Fischbach K., Preim B.: Robust cardiac function assessment in 4D PC-MRI data of the aorta and pulmonary artery. *CGF 35*, 1 (2016), 32–43. doi:10.1111/cgf.12669. 4

[LS10] Liu J., Sun J.: Parallel graph-cuts by adaptive bottom-up merging. In *Proc: IEEE CVPR* (2010), pp. 2181–8. doi:10.1109/CVPR.2010.5539898. 3

[LSJW15] Loecher M., Schrauben E., Johnson K. M., Wieben O.: Phase unwrapping in 4D MR flow with a 4D single-step Laplacian algorithm. *J Magn Reson Imag 43*, 4 (2015), 833–42. doi:10.1002/JMRI.25045. 3

[NNB*15] Nayak K. S., Nielsen J.-F., Bernstein M. A., Markl M., Gatehouse P. D., Botnar R. M., Saloner D., Lorenz C., Wen H., Hu B. S., Epstein F. H., Oshinski J. N., Raman S. V.: Cardiovascular magnetic resonance phase contrast imaging. *J Cardiovasc Magn Reson 17*, 71 (2015), 1–26. doi:10.1186/s12968-015-0172-7. 2

[OLK*14] Oeltze S., Lehmann D. J., Kuhn A., Janiga G., Theisel H., Preim B.: Blood flow clustering and applications in virtual stenting of intracranial aneurysms. *IEEE TVCG 20*, 5 (2014), 686–701. doi:10.1109/TVCG.2013.2297914. 3, 9

[PMvN14] Potters W. V., Marquering H. A., vanBavel E., Nederveen A. J.: Measuring wall shear stress using velocity-encoded MRI. *Curr Cardiovasc Imag Report 7*, 4 (2014), 1–12. doi:10.1007/s12410-014-9257-1. 7

[RBM*18] Raghav V., Barker A. J., Mangiameli D., Mirabella L., Markl M., Yoganathan A. P.: Valve mediated hemodynamics and their association with distal ascending aortic diameter in bicuspid aortic valve subjects. *J Magn Reson Imag 47*, 1 (2018). doi:10.1002/JMRI.25719. 2

[SAG*14] Stankovic Z., Allen B. D., Garcia J., Jarvis K. B., Markl M.: 4D flow imaging with MRI. *J Cardiovasc Diag Ther 4*, 2 (2014), 173–92. doi:10.3978/j.issn.2223-3652.2014.01.02. 2

[SDW*15] Sigovan M., Dyverfeldt P., Wrenn J., Tseng E. E., Saloner D., Hope M. D.: Extended 3D approach for quantification of abnormal ascending aortic flow. *J Magn Reson Imag 33*, 5 (2015), 695–700. doi:10.1016/j.mri.2015.02.020. 2

[TZG96] Taubin G., Zhang T., Golub G. H.: Optimal surface smoothing as filter design. In *Proc: ECCV*. 1996, pp. 283–92. doi:10.1007/BFb0015544. 3

[VJtV12] Van Pelt R. F. P., Jacobs S. S. A. M., ter Haar Romeny B. M., Vilanova A.: Visualization of 4D blood-flow fields by spatiotemporal hierarchical clustering. *CGF 31*, 3 (2012), 1065–74. doi:10.1111/j.1467-8659.2012.03099.x. 3

[WSW96] Wigström L., Sjöqvist L., Wranne B.: Temporally resolved 3D phase-contrast imaging. *J Magn Reson Imag 36*, 5 (1996), 800–3. doi:10.1002/mrm.1910360521. 2

[YWM07] Yu H., Wang C., Ma K.-L.: Parallel hierarchical visualization of large time-varying 3D vector fields. In *Proc: IEEE Supercomput* (2007), pp. 1–12. doi:10.1145/1362622.1362655. 3